

# Pyrrolic-structure enriched nitrogen doped graphene for highly efficient next generation supercapacitors

Cite this: *J. Mater. Chem. A*, 2013, **1**, 2904

Fathy M. Hassan, Victor Chabot, Jingde Li, Brian Kihun Kim, Luis Ricardez-Sandoval\* and Aiping Yu\*

This study reports the preparation of pyrrolic-structure enriched nitrogen doped graphene by hydrothermal synthesis at varied temperature. The morphology, structure and composition of the prepared nitrogen doped graphene were confirmed with SEM, XRD, XPS and Raman spectroscopy. The material was tested for supercapacitive behavior. It was found that doping graphene with nitrogen increased the electrical double layer supercapacitance to as high as  $194 \text{ F g}^{-1}$ . Furthermore, density functional theory (DFT) calculations showed the proper level of binding energy found between the pyrrolic-nitrogen structure and the electrolyte ions, which may be used to explain the highest contribution of the pyrrolic-structure to the capacitance.

Received 12th November 2012  
Accepted 19th December 2012

DOI: 10.1039/c2ta01064j

[www.rsc.org/MaterialsA](http://www.rsc.org/MaterialsA)

## 1 Introduction

Supercapacitors are devices that can store greater amounts of energy than conventional capacitors, and they are able to deliver more power than batteries. Furthermore, they have relatively long cycle life and are capable of rapidly charging or discharging at high power density.<sup>1,2</sup> There is significant interest to increase the use of supercapacitors in a wide and growing range of applications including electric vehicles, electric utilities, backup power and more.<sup>2-4</sup> Various materials have been used as electrode materials for supercapacitors including carbon materials,<sup>5-9</sup> metal oxides<sup>10-12</sup> or conducting polymers.<sup>13</sup> However, carbon in its various forms is the most common electrode material for supercapacitor applications that require high capacitance and high power density. Graphene, the 2D carbon nanostructure, has attracted great interest for application in the field of energy storage and conversion.<sup>14-17</sup> Its excellent and unique properties *e.g.* high chemical stability,<sup>18,19</sup> high electrical conductivity<sup>20,21</sup> and large surface area<sup>21,22</sup> enable its use for many potential applications,<sup>23,24</sup> including supercapacitors<sup>16,25</sup> or Li batteries.<sup>26</sup>

Many attempts have been made to modify graphene properties by controlling its structure. The success of doping carbon nanotubes with nitrogen<sup>27-29</sup> encouraged the trials for chemical doping of graphene with heteroatoms such as N. This was found to be an effective method to intrinsically modify graphene since nitrogen chemically binds to the carbon lattice of graphene. Further, nitrogen has a comparable atomic size and high electronegativity compared to carbon.<sup>30,31</sup> Nitrogen doped graphene

(NG) can be synthesized by a CVD approach where the nitrogen containing precursors are introduced to graphene at high temperature with controlled atmosphere.<sup>26,31</sup> Other methods include nitrogen plasma treatment<sup>32</sup> or DC arc-discharge.<sup>33</sup> The NG produced from these methods exhibits four different types of nitrogen bonding configurations: pyridine-like (N-6, 398.1–398.3 eV), pyrrole-like (N-5, 399.8–401.2 eV), quaternary (N-Q, 401.1–402.7 eV), and oxidized nitrogen (N-O, 403–405 eV). There are limited experimental or modelling studies available that investigate the difference of these four different nitrogen configurations and their contribution to supercapacitor performance.<sup>30,34</sup>

It is reported that NG prepared from the identified methods contain predominantly N-6 configured nitrogen.<sup>31,32</sup> In this paper we introduce an approach to produce NG using a hydrothermal method and systematically study the temperature impact on nitrogen configuration and performance. In addition, the graphene synthesized by this approach is more enriched with nitrogen in the N-5 configuration. The morphology and the introduction of nitrogen to the graphene were confirmed by SEM, XRD, Raman and XPS spectroscopy. The maximum supercapacitor performance was found using the NG sample prepared at  $130 \text{ }^\circ\text{C}$ . Meanwhile, density functional theory (DFT) calculations were carried out to study the binding energy between different nitrogen configurations and the electrolyte, which gives insight required to better understand the contribution from each nitrogen configuration.

## 2 Experimental

### 2.1 Synthesis of graphitic oxide

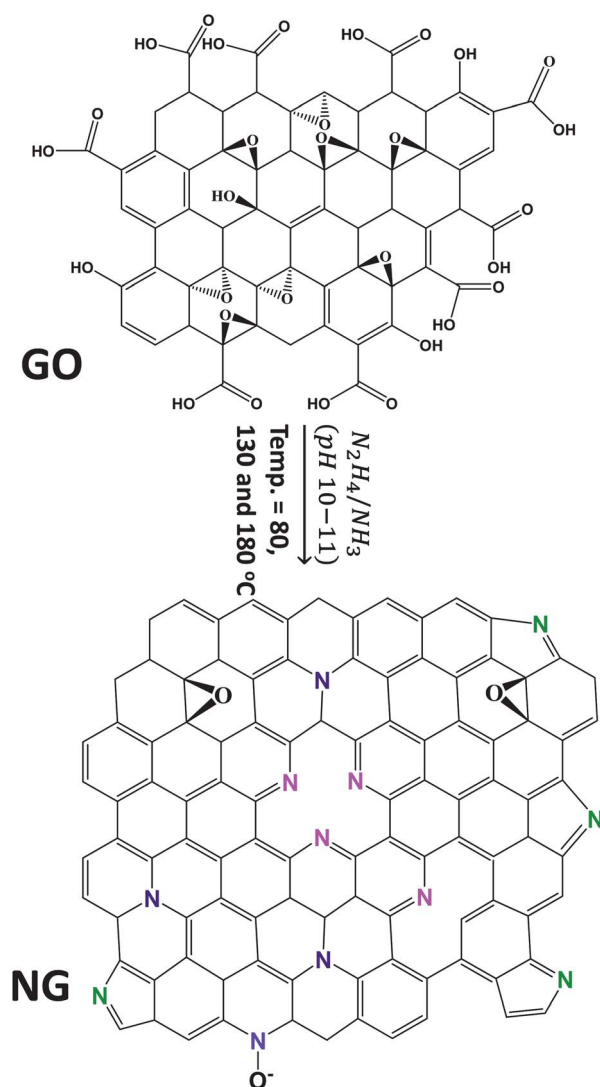
The graphite oxide (GO) was prepared following the modified Hummers' method in which graphite flakes are oxidized using a

Department of Chemical Engineering, Waterloo Institute for Nanotechnology, Waterloo Institute for Sustainable Energy, University of Waterloo, 200 University Avenue West, Waterloo, Ontario, Canada N2L 3G1. E-mail: [aipingyu@uwaterloo.ca](mailto:aipingyu@uwaterloo.ca); [laricard@uwaterloo.ca](mailto:laricard@uwaterloo.ca)

mixture of potassium permanganate, sulfuric acid and sodium nitrate.<sup>35</sup> In a typical synthesis 2 g of graphite powder and 1 g of sodium nitrate were stirred into 46 mL of conc. H<sub>2</sub>SO<sub>4</sub> in a round bottom flask while keeping the temperature at 0 °C using an ice bath. 6 g of KMnO<sub>4</sub> were added slowly and then the mixture was diluted by deionized water, followed by the addition of 40 mL of 30% H<sub>2</sub>O<sub>2</sub>. After that, the mixture was filtered, washed and dried.

## 2.2 Synthesis of NG

Scheme 1 shows the hydrothermal synthesis of NG. In brief, a 2 mg mL<sup>-1</sup> solution of graphitic oxide in deionized water was made and sonicated for an hour. Then, the pH was adjusted to 10–11 using an ammonia solution before adding 1.75 mL of aqueous hydrazine. The mixture was magnetically stirred for 10 minutes, transferred to a Teflon-lined autoclave and subjected to hydrothermal treatment for 3 hours. After cooling, the mixture was filtered, washed with deionized water and dried in a vacuum oven. For the preparation of pristine graphene,



**Scheme 1** Hydrothermal reduction/doping of GO to NG.

NaBH<sub>4</sub> was used following our previous procedure<sup>36</sup> instead of using ammonia and hydrazine. The rest of the reaction conditions were kept the same as that of NG. Three different temperatures including 80 °C, 130 °C and 180 °C were investigated to determine the temperature effect. Correspondingly, the products were denoted as NG80, NG130, and NG180, respectively.

## 2.3 Physical characterizations

Morphology of the NG materials was characterized by scanning electron microscopy (SEM) (LEO FESEM 1530) and transmission electron microscopy (TEM) (Philips CM300). XRD patterns were recorded by a Bruker-AXS D8 Discover diffractometer (Co-K $\alpha$  source). X-ray photoelectron spectroscopy (XPS) was conducted to determine the atomic composition using a Thermal Scientific K-Alpha XPS spectrometer. Raman scattering spectra were recorded on a HORIBA Scientific LabRAM HR system (532.4 nm laser).

## 2.4 Electrochemical measurements

Electrochemical measurements were carried out using a CHI 760D electrochemical workstation (CH Instruments, USA). Cyclic voltammetry (CV), charge discharge (CD), and electrochemical impedance spectroscopy (EIS) techniques were all carried out following a 25-cycle CV activation between  $-0.1$  and  $0.9$  V *versus* SCE at a scan rate of  $0.1$  V s<sup>-1</sup> in  $1$  M KCl electrolyte. CV was carried out between  $-0.1$  and  $0.9$  V *versus* SCE at scan rates between  $0.01$  and  $0.2$  V s<sup>-1</sup>. Working electrodes were prepared by pipetting an aqueous  $2$  mg mL<sup>-1</sup> dispersion of NG onto glassy carbon. Charge-discharge (CD) was carried out between  $-0.1$  and  $0.9$  V *versus* SCE at current densities between  $0.5$  and  $1$  A g<sup>-1</sup>. The capacitance of the three electrode super-capacitor cells was calculated based on the mass of the graphene or NG within the electrodes.

## 2.5 Computational methods

The cluster calculations were based on the unrestricted Kohn-Sham DFT approach and were carried out with the program ADF<sup>37,38</sup> on SHARCNET (<http://www.sharcnet.ca>) under the umbrella of Compute/Calcul Canada. In ADF, the electron wave functions were developed on a basis set of numerical atomic orbitals (NAOs) and of Slater type orbitals (STOs). The calculations were performed by using Perdew–Burke–Ernzerhof (PBE) generalized gradient correction of the exchange-correlation function. The triple polarization (TZP) basis of Slater-type orbitals provided with the ADF package was used. In order to describe the interactions between the potassium ion (K<sup>+</sup>) and the graphene, the bonding energies (BE) of K<sup>+</sup> ion were defined by the following equation:

$$BE = E_{(\text{graphene})} + E_{(\text{K}^+)} - E_{(\text{K}^+-\text{graphene})} \quad (1)$$

where  $E(\text{K}^+-\text{graphene})$ ,  $E(\text{K}^+)$ , and  $E(\text{graphene})$  represent the energies of the K<sup>+</sup>-bound to the graphene structure, the K<sup>+</sup> ion, and the graphene structure, respectively.

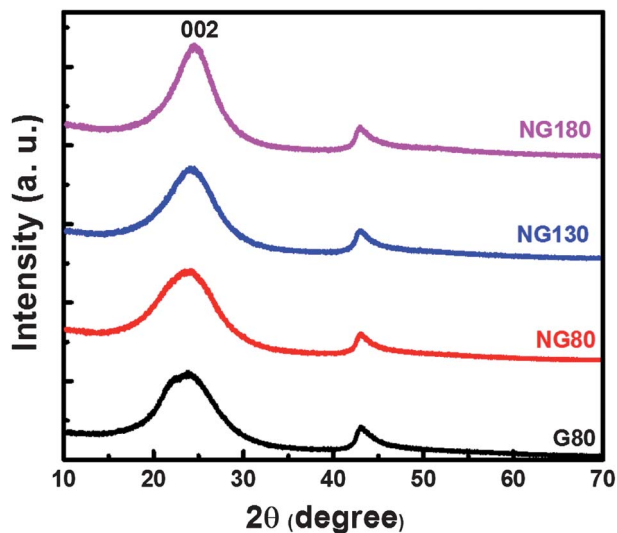


Fig. 1 XRD for NG samples prepared at different temperatures in comparison with pristine graphene.

### 3 Results and discussion

#### 3.1 Structure and morphology characterization

Fig. 1 shows the XRD results of NG prepared at different temperatures with comparison to the pristine graphene, G80. The figure shows a major peak (002) at about  $24 \pm 0.2^\circ$  which corresponds to an average interlayer spacing of 3.79, 3.73, 3.67, and 3.62 Å for G80, NG80, NG130, and NG180 respectively. These spacing values are a little greater than that of graphite ( $\sim 3.36$  Å) due to doping with nitrogen and oxygen. It is interesting to note that by doping and by increasing the doping temperature the  $d$ -spacing decreases in the investigated temperature range. It is expected that by increasing the temperature more functional groups are removed (especially those that extend off the basal plane leading to lattice mismatch in the reduced graphene). This is expected to cause a slight decrease in the  $d$ -spacing as is observed here. In addition, the broadening of the peaks is evidence for the exfoliation and conversion of graphitic oxide into graphene and NG. Around  $43^\circ$  there are weak diffraction peaks that correspond to (004) and/or (100) planes. The crystal size ( $L_c$ ) was estimated using the Scherrer equation;<sup>39</sup>

$$L_c = A\lambda / (B \cos \theta) \quad (2)$$

where  $A$  is the shape factor ( $\sim 0.9$ );  $\lambda$  is the X-ray wavelength;  $\theta$  the Bragg angle;  $B$  is the full width at half maximum (FWHM) of

Table 1 List of parameters deduced from XRD data for different materials

	$2\theta$ , degree	$d$ -spacing, Å	FWHM, radian	$L_c$ , Å	No. of layers
G80	23.48	3.79	0.0836	13.13	3.46
NG80	23.86	3.73	0.0925	13.23	3.55
NG130	24.24	3.67	0.1071	15.33	4.18
NG180	24.63	3.62	0.1079	16.98	4.69

the (002) peak in radians. The results are listed in Table 1. The crystallite size increased slightly on introduction of nitrogen at  $80^\circ\text{C}$  from G80 to NG80. However, the increase in  $L_c$  becomes more significant by increasing the temperature.  $L_c$  is based on the (002) peak and reflects the  $Z$  dimension of the graphene plates (thickness). Dividing the  $L_c$  with the corresponding  $d$ -spacing of the material gives an estimation of the number of layers;<sup>31,40</sup> this is listed in Table 1.

Fig. 2a shows an FE-SEM image of NG180. The figure shows an exfoliated and wrinkled nanoplatelet texture characteristic for graphene. Fig. 2b displays high resolution TEM image for NG180. The image shows that the NG prepared by this hydrothermal method is reasonably exfoliated and is formed of a few layers thick. This was shown by XRD to be 3 to 4 layers.

Fig. 3 displays the UV-Vis absorption spectra of the different materials after dispersion in solution as shown in the onset. The graphitic oxide solution has more absorption than graphene. This is attributed to the greater number of functional groups in GO compared to that of G. For the NG materials, the absorbance increases with increased doping temperature. Tauc's equation was used to determine the energy band gap,  $E_g$ ;

$$\omega^2 \varepsilon = (h\omega - E_g)^2 \quad (3)$$

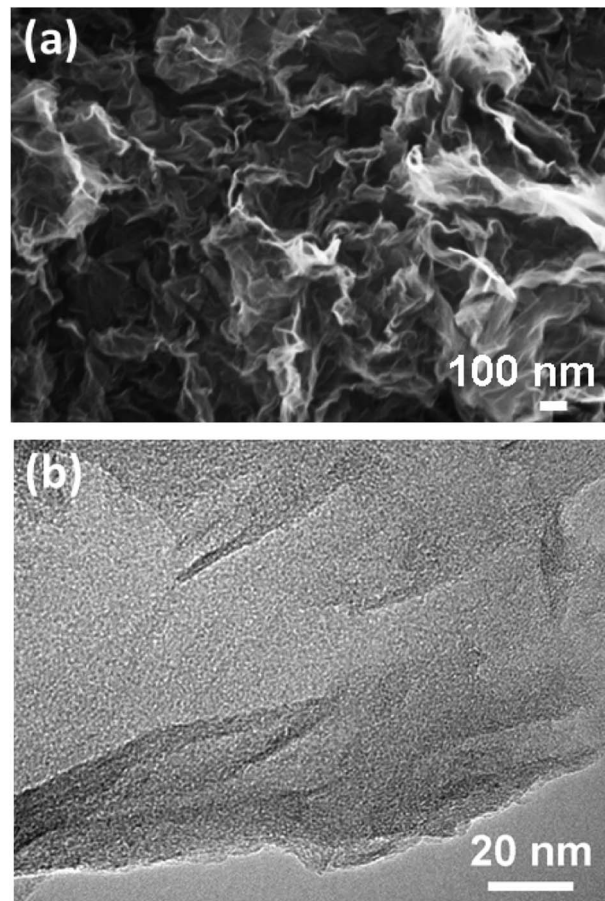


Fig. 2 SEM micrograph of NG180 (a) and the corresponding high resolution TEM image (b).

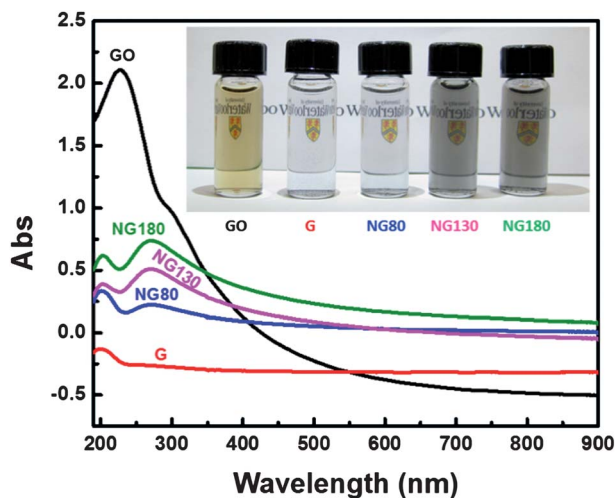


Fig. 3 UV absorption data for different materials.

Table 2 Band gap of different materials as determined using eqn (3) and Fig. 3

Band gap	G80	NG80	NG130	NG180
$E_g$ (eV)	1.62	2.85	1.80	2.10

where  $\varepsilon$  is the absorbance,  $\omega$ , is the angular frequency of light, which is  $\frac{2\pi}{\lambda}$ , and  $\lambda$  is the wavelength. On plotting  $\frac{\varepsilon^{1/2}}{\lambda}$  versus  $\frac{1}{\lambda}$ , and extrapolating the obtained straight line segment until intersecting with the x-axis, we can get the band gap. Table 2 lists the band gap of the different materials. It is interesting to note that NG130 has the smallest energy band gap, suggesting it has the highest intrinsic conductivity among the NG materials. This could relate to the supercapacitor performance of the material since higher conductivity material usually results in lower internal resistance of the electrode.

Fig. 4 displays the results of the Raman spectra of NG samples in comparison with pristine graphene. The Raman spectra parameters are listed in Table 3 for different materials.

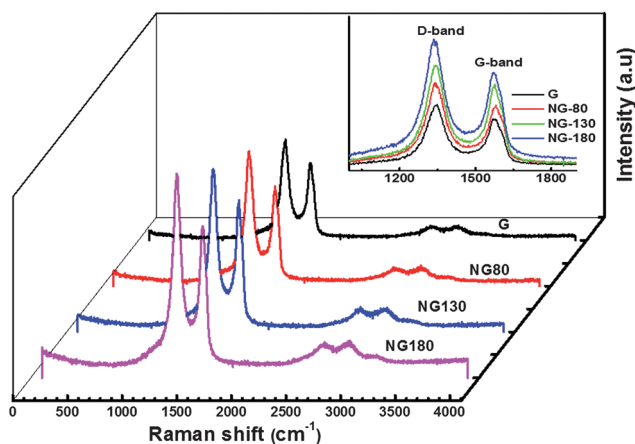


Fig. 4 Raman spectroscopy of the NG samples prepared at different temperatures in comparison with pristine graphene.

Table 3 Parameters estimated from Raman spectroscopy for different materials

Materials	D-Band	G-band	$I_D/I_G$	$I_{2D}/I_G$	$L_a$ , nm
G80	1341.8	1575.5	1.27	4.22	15.18
NG80	1338.9	1578.4	1.36	4.23	14.18
NG130	1340.4	1575.5	1.24	0.21	15.55
NG180	1334.6	1572.6	1.34	0.25	14.39

The spectra show the typical D, G and 2D band of both graphene and NG. The presence of the D band peak as well as the very weak 2D band is a typical characteristic of chemically synthesized graphene.<sup>41–43</sup> The G band is attributed to the first order scattering of the stretching vibration mode  $E_{2g}$  observed for the  $sp_2$  carbon domain. The D band is strongly associated with the degree of disorder within the graphene.<sup>44</sup>

A quantitative measure to estimate the degree of disorder in graphene is the ratio of intensities of the D and G bands *i.e.*  $I_D/I_G$ .<sup>42,43</sup> The values for  $I_D/I_G$  are 1.27, 1.36, 1.24 and 1.34 for G80, NG80, NG130, and NG180, respectively. This implies that the doped graphene in general has higher values of  $I_D/I_G$  than the pristine graphene, which means possessing more defects, than the pristine graphene. An exception of this is NG130 which shows the lowest value for  $I_D/I_G$ . The possible reason for this might be attributed to structural differences. Since the nitrogen content for NG130 is similar to that of NG180, about 2.77 atom%, the difference might be in the configuration of bonds and/or the nature of N doped to graphene, as will be seen later by XPS measurements. It is also interesting to note the values of  $I_{2D}/I_G$ , which is inversely related to the charge carrier concentration. Here the values for  $I_{2D}/I_G$  are 4.22, 4.23, 0.21, and 0.25 for G80, NG80, NG130, and NG180, respectively, see Table 3. The results indicate that the value decreases by increasing the temperature from 80 °C to 130 °C or 180 °C. This reveals that increasing the temperature of the synthesis generally improves the conductivity of the doped graphene. However, the value of  $I_{2D}/I_G$  is the smallest for NG130 indicating that this sample has higher charge carrier concentration, which means that it is more conductive and is in agreement with it having the smallest band gap as seen from the UV-vis data. It has been shown that the ratio  $I_D/I_G$  is inversely related to the in-plane crystallite size  $L_a$ , which can be determined using the Tuinstra–Koenig relationship:<sup>45</sup>

$$L_a(\text{nm}) = (2.4 \times 10^{-10})\lambda^4 \left( I_D/I_G \right)^{-1} \quad (4)$$

where  $\lambda$  is the Raman excitation wavelength. The values of  $L_a$  are listed in Table 3, corresponding to the interdefect distance on the surface of the graphene sheets.<sup>30</sup>

Fig. 5a compares the XPS results of the pristine graphene (G80) and the nitrogen doped graphene (NG130). The figure clearly shows the appearance of a peak at about 400 eV which corresponds to nitrogen. In addition, there is some residual oxygen in both samples, which is common for the solution prepared graphene. The percentage of doped nitrogen was estimated by XPS analysis to be 3.20, 2.77, 2.77 atom% for NG80, NG130 and NG180 respectively. Fig. 5b–d show high resolutions of the nitrogen for the samples NG80, NG130 and NG180. The

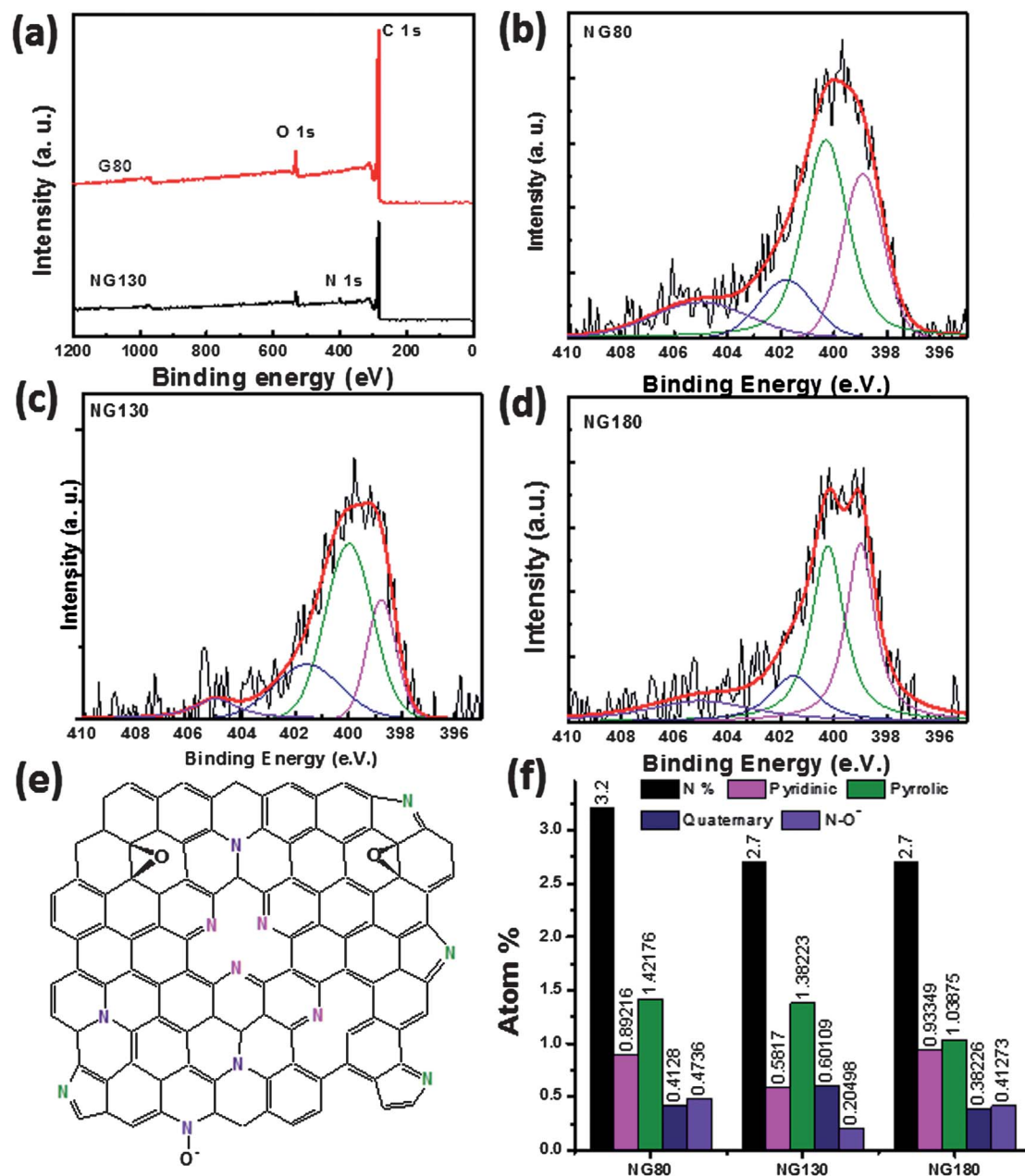


**Fig. 5** (a) XPS spectra for NG prepared at 130 °C and pristine graphene; (b), (c) and (d) high resolution XPS for different NG samples prepared at 80, 130, and 180 °C, respectively; (e) is a proposed NG structure based on the result of XPS analysis; and (f) is atomic% of nitrogen in every NG sample and its associated resolved components in atom%. The black bar is the total atomic% of nitrogen in that sample.

results of fitting of these spectra show that nitrogen bonds to the graphene matrix in four different forms including pyridinic, pyrrolic, quaternary (graphitic) and oxidized nitrogen, which are centered at 398.9, 400.3, 401.8 and 405 eV,<sup>46–48</sup> respectively. The suggested structure is shown in Fig. 5e and the percentages of these nitrogen components are plotted in Fig. 5f. In all samples, the pyrrolic nitrogen predominates. However, for NG130 the ratio of the pyrrolic nitrogen to the overall nitrogen is the highest.

### 3.2 Electrochemical measurements

Fig. 6a shows the cyclic voltammetry curves for NG prepared at different temperatures with a scan rate of 100 mV s<sup>-1</sup> in 1 M KCl.

The CV curves are virtually rectangular, showing that an approach to ideal and reversible capacitive behavior is almost achieved.<sup>36</sup> The loop area for NG130 is greatest, followed by NG180 and then NG80 has the smallest area. Fig. 6b shows the effect of scan rate on the CV for the NG130 electrodes. The general trend observed is that as the scan rate increases the area of the CV loop increases. The specific capacitance of the different electrode materials is determined based on their CVs according to the following equation:

$$C_s = \frac{\int idV}{2 \times m \times \Delta V \times S} \quad (5)$$

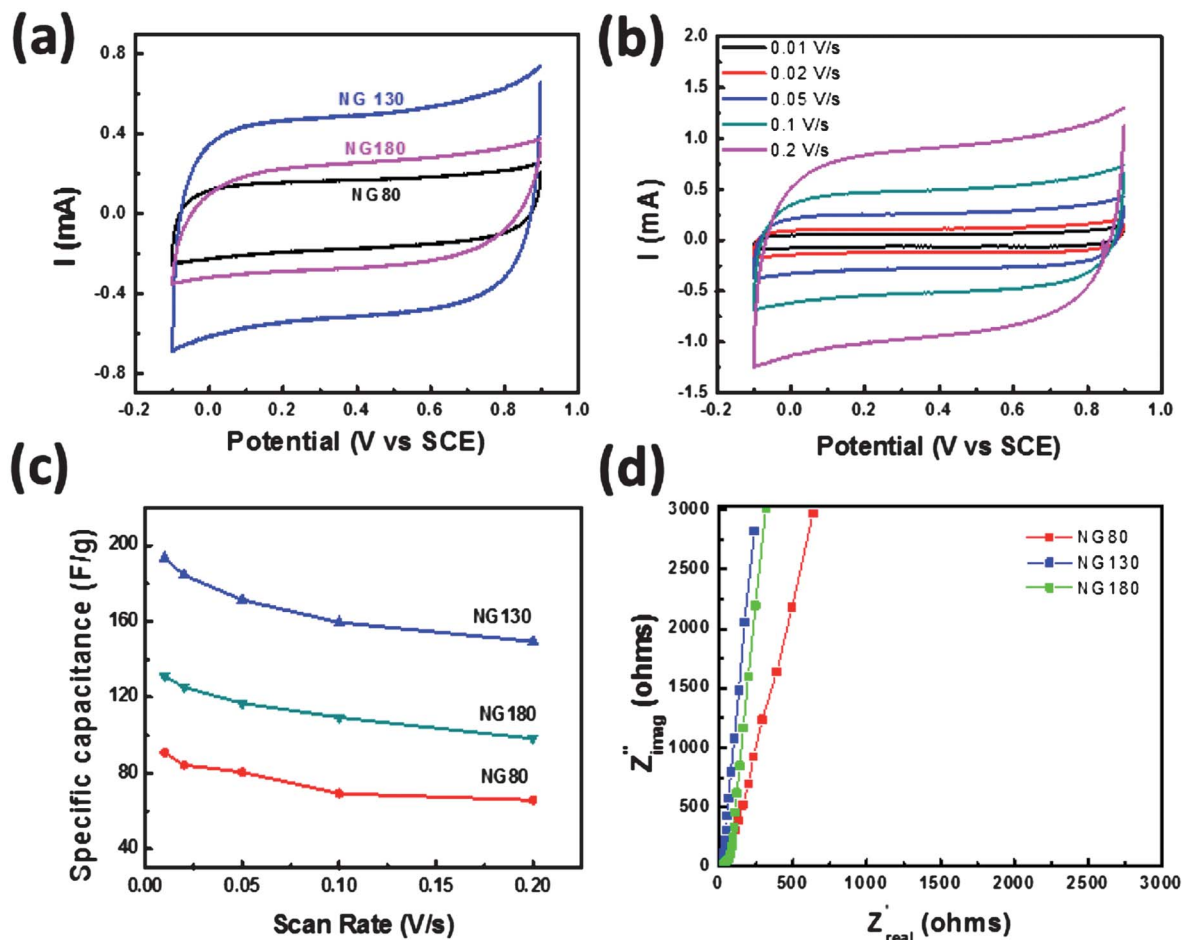


**Fig. 6** (a) CV curves for NG samples prepared at different temperatures measured at  $100 \text{ mV s}^{-1}$  in  $1 \text{ M KCl}$ , (b) CV curves for NG130 at different scan rates, (c) the capacitance of the different materials as a function of the scan rate, and (d) the EIS of the different NG electrodes.

where  $C$  is the specific capacitance in farads per gram,  $\int i dV$  is the integrated area under the CV curve,  $m$  is the mass of the electrode active materials in grams,  $\Delta V$  is the scanned potential window in volts, and  $S$  is the scan rate in volts per seconds. The results of these calculations are plotted in Fig. 6c. The results show that nitrogen doping graphene clearly increases its capacitive behavior. The reason may be attributed to the high electronegativity of nitrogen which helps create dipoles on the surface of graphene, resulting in higher tendency to attract charged species to the surface. The highest performance achieved here is for NG130 which shows a capacitance of  $194 \text{ F g}^{-1}$ . It is noteworthy that NG130 has the smallest band gap, the smallest  $I_D/I_G$  ratio, the highest predicted charge carrier concentration (based on the smallest  $I_{2D}/I_G$ ), and the highest proportion of pyrrolic nitrogen to the overall nitrogen. This interesting result is further confirmed by EIS measurements of the different NG electrodes shown in Fig. 6d. The figure shows the Nyquist plots for the three different electrode materials: NG80, NG130, and NG180. The linearity in the EIS plots at low frequency suggests that the electrode process is under diffusion control. The slope of these lines is related to the formation rate of the electric double layer (EDL). The larger the slope the faster the EDL will be formed.<sup>49,50</sup> The slope for the NG130 electrode is

obviously greater than that for the NG180 and NG80 electrodes, which further emphasizes that NG130 shows a more ideal supercapacitor behavior. The three electrodes shows semi-circles at the high frequency with very small diameters, suggesting a small charge transfer resistance.

Fig. 7a shows the galvanostatic charge–discharge behavior of the NG130 electrodes at different current densities. The nearly ideal behavior as electrical double layer capacitor (EDLC) is visibly seen throughout the linear charge–discharge slopes as well as the symmetry observed for the curves. The capacitance values were calculated from the slopes of the discharge curves following the equation  $C_s = I_s/(\Delta V/\Delta t)$ . The results were plotted in Fig. 7b. It can clearly be seen that NG130 has the highest capacitance at all currents. The trend of increasing specific capacitance is comparable to that calculated from the CV measurements, see Table 4.

For supercapacitors, energy and power densities are two important parameters to consider. However, it should be noted that performance calculations based on a three-electrode system can often overstate material performance in real devices due to the low weight loading on the electrode. Therefore, the energy density estimate for an equivalent two electrode cell composed of NG130 is calculated using the following equation:<sup>51,52</sup>

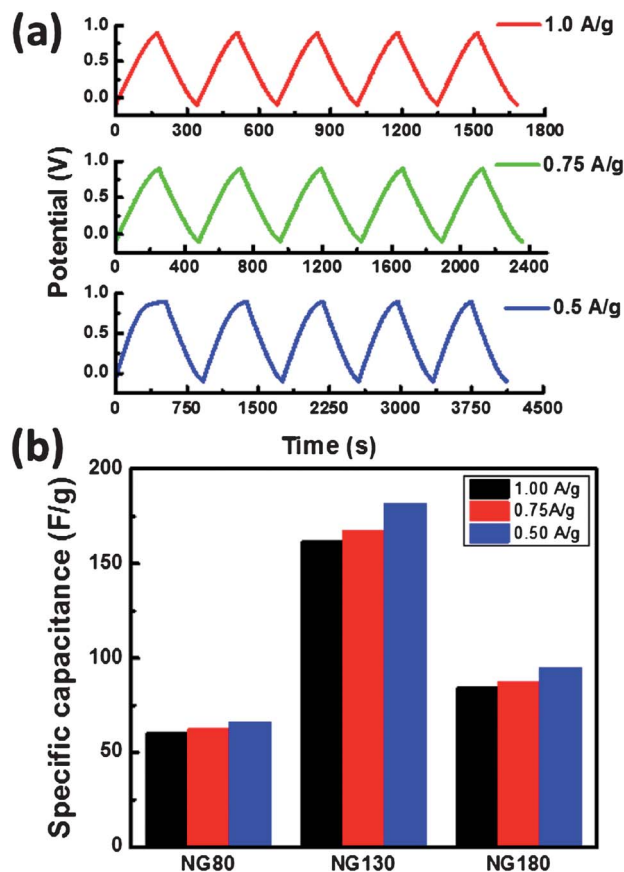


**Fig. 7** (a) Galvanostatic charge–discharge curves for NG130 electrode at different currents and (b) the capacitances derived from the CD curves for the different NG materials at different currents.

$$E = (C_s/4) \times (\Delta V)^2/7.2 \quad (6)$$

where  $C_s/4$  is the specific capacitance estimate of a two electrode cell in farads per gram,<sup>53</sup>  $\Delta V$  is the potential window for CV measurements in volts, and  $E$  is the energy density in  $\text{W h kg}^{-1}$ . Utilizing the three electrode test data from the CV measurements, the maximum energy densities (measured at a scan rate of  $0.01 \text{ V s}^{-1}$ ) of a two-electrode cell are estimated to be 6.7 and  $3.2 \text{ W h kg}^{-1}$  for NG130 and graphene respectively. The maximum average power densities of the electrodes were calculated using the energy densities and the discharge time  $t$ , from CV at  $0.2 \text{ V s}^{-1}$ , using the following equation:<sup>54</sup>

$$P = \frac{E}{t} \quad (7)$$

**Table 4** Specific supercapacitances of different NG calculated from CV results at  $0.01 \text{ V s}^{-1}$ , and from CD results at  $0.5 \text{ A g}^{-1}$

Material	$C_s$ , from CV at $0.01 \text{ V s}^{-1}$ ( $\text{F g}^{-1}$ )	$C_s$ , from CD at $0.5 \text{ A g}^{-1}$ ( $\text{F g}^{-1}$ )
G80	91	53
NG80	94	66
NG130	194	182
NG180	131	95

The calculated values for average power density were found to be  $3.7 \text{ kW kg}^{-1}$  and  $1.6 \text{ kW kg}^{-1}$  for NG130 and G80, respectively. This result indicates that doping graphene with nitrogen almost doubles the power density that could be obtained utilizing this material.

In order to better understand the contribution of capacitance from each nitrogen configuration and further explore the reason of the best performance demonstrated by NG130 at a molecular level. We carried out the DFT calculations to estimate the binding energy between the nitrogen configurations and  $\text{K}^+$  ions. In the present study, the graphene surface was modeled using a hydrogenated graphene cluster ( $\text{C}_{54}\text{H}_{18}$ ) (Fig. 8) with C–C and C–H bond distances equal to the values obtained for bulk graphite that are 1.42 and 1.09 Å,<sup>55</sup> respectively. In all the calculations, the clusters were allowed to relax. A set of stable configurations for  $\text{K}^+$  ion adsorption on the N-configurations based on first principles density functional theory (DFT) are shown in Fig. 9. The corresponding binding energies of each configuration are also shown. The results in Table 5 show that adsorption of the  $\text{K}^+$  ion on N-Q has the smallest bonding energy, followed by N-5, N-O<sup>−</sup> and N-6. Among all the N-configurations, strong bonding energies were observed for  $\text{K}^+$  ion on the N-6 and N-O<sup>−</sup> structures:  $-2.06 \text{ eV}$  on the N-6 with three pyridinic nitrogen atoms,  $-1.92 \text{ eV}$  on the N-6 with three pyrrolic nitrogen atoms, and  $-1.34 \text{ eV}$  on N-O<sup>−</sup>.

From the XPS results we have seen that in all nitrogen doped samples the pyrrolic carbon dominates. In addition, NG130 has the highest percentage of pyrrolic nitrogen among all the samples. Based on the calculation, the pyridinic nitrogen (Table 5) has the strongest binding to the  $\text{K}^+$  ions, whether in a 3 pyridinic unit cell or a one pyridinic unit cell. Whereas pyrrolic N binding to  $\text{K}^+$  only gives rise to  $-1.05 \text{ eV}$ . The strong bonding is due to attraction of ions, but if the attraction is too strong, releasing of the ions becomes difficult. Therefore, NG130 has the most optimized wettability to the  $\text{K}^+$  ions. If we compare the contribution of the ions approaching the surface to binding we can say overall that pyrrolic nitrogen is readily accessible to ions. This observation might explain why electrodes fabricated

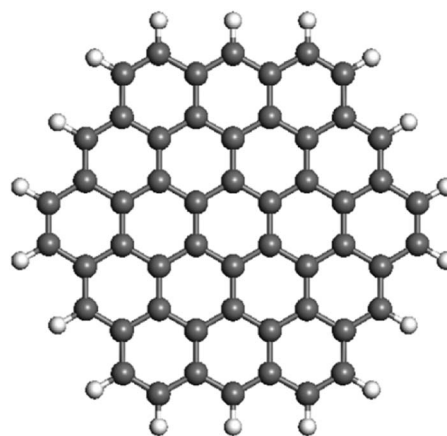


**Fig. 8** Structure of the graphene model ( $\text{C}_{54}\text{H}_{18}$ ) used in the present study. The edge region of graphene is terminated by hydrogen atoms. The larger gray circles are carbon atoms, and the smaller white circles are hydrogen atoms.

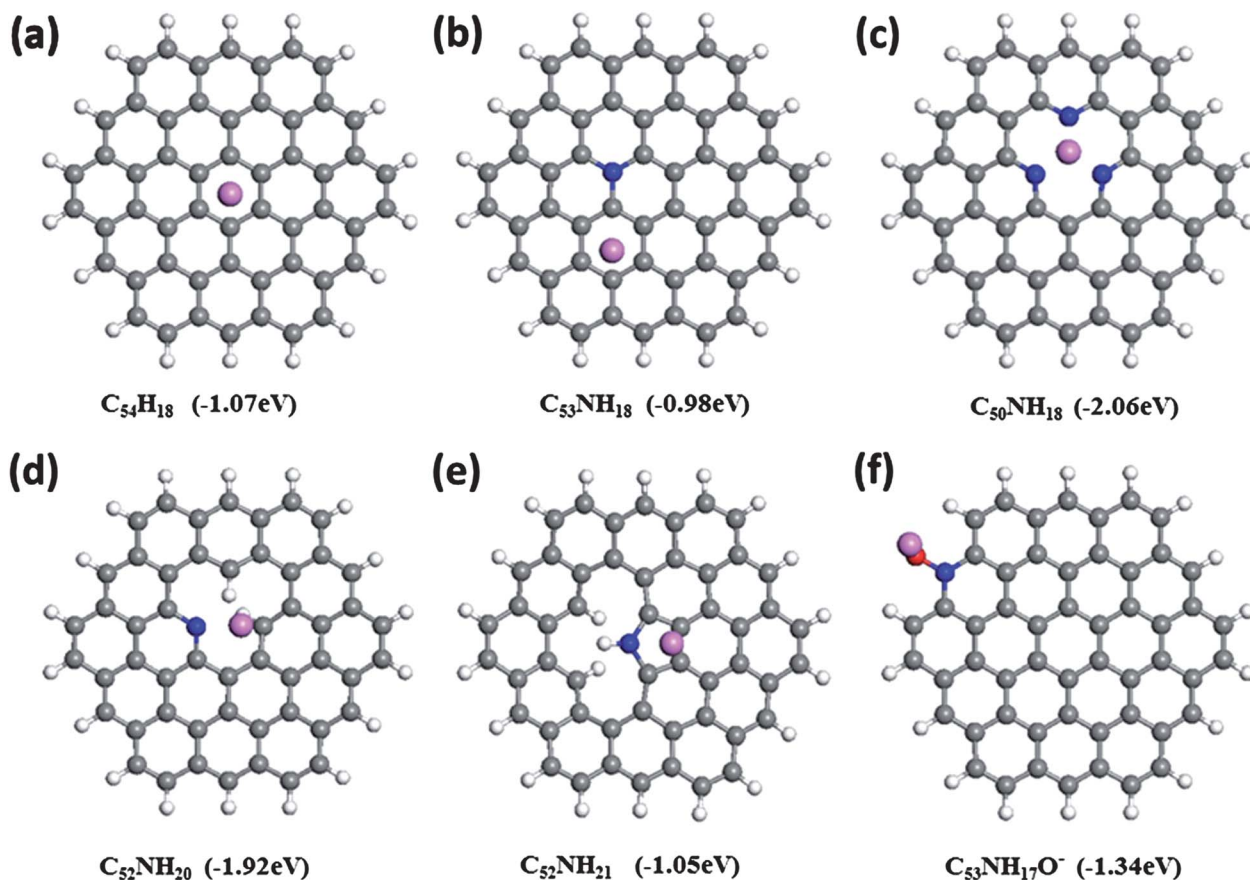


**Fig. 9** Optimized  $K^+$ -bound structures and binding energies on different N-doped graphene configurations: (a) graphene, (b) N-Q, (c) three N-6, (d) N-6 with H-terminated dangling bonds, (e) N-5 with H-terminated dangling bonds, (f) N-5 anion with H-terminated dangling bonds, and (f) N-O<sup>-</sup> (grey, blue, and white represent C, N, and H atoms, respectively; pink and red stand for  $K^+$  and  $O^-$ , respectively).

**Table 5** Binding energies between  $K^+$  ions and different N configurations obtained from DFT calculations

Nitrogen configuration	N-6 <sup>a</sup>	N-6 <sup>b</sup>	N-5	N-Q	N-O <sup>-</sup>
BE (eV)	-2.06	-1.92	-1.05	-0.98	-1.34

<sup>a</sup> N-6 with three pyridinic nitrogen (see Fig. 9c). <sup>b</sup> N-6 with H-terminated dangling bonds (see Fig. 9d).

from NG130 shows the highest capacitance. It is also important to predict that if the strong binding species predominate, the charge will bind to the surface too tightly which affect its reversibility. Consequently, the supercapacitor loses Coulombic efficiency.

## 4 Conclusions

Graphene and nitrogen doped graphene have been synthesized by a hydrothermal technique from graphitic oxide. XPS confirmed that the percentage of doping was 2.77–3.2%. In addition, among the different nitrogen species, pyrrolic nitrogen was found to predominate. The doping was found to significantly enhance the specific capacitance, partially due to the improved electrical conductivity of the materials. This is in

agreement with the lower band gap and lower impedance results among the NG series. The temperature was found to have a varied effect on the performance and the optimized results were achieved at 130 °C with a high supercapacitance of 194 F g<sup>-1</sup>. Energy density was estimated to be as high as 6.7 W h kg<sup>-1</sup> and the maximum power density reached 3.7 kW kg<sup>-1</sup>. Density functional theory applied to study the binding energy between different nitrogen configurations and the electrolyte suggests that the pyrrolic configuration contributes more to the capacitance due to it having more optimal binding energy than the electrolyte ions. This material is an excellent candidate for use in electrical double layer supercapacitors.

## Acknowledgements

This research was financially supported by the Natural Sciences and Engineering Research Council of Canada (NSERC) as well as the University of Waterloo.

## Notes and references

- 1 C. Merlet, B. Rotenberg, P. A. Madden, P.-L. Taberna, P. Simon, Y. Gogotsi and M. Salanne, *Nat. Mater.*, 2012, **11**, 306–310.

- 2 P. Simon and Y. Gogotsi, *Nat. Mater.*, 2008, **7**, 845–854.
- 3 M. D. Stoller, S. Park, Y. Zhu, J. An and R. S. Ruoff, *Nano Lett.*, 2008, **8**, 3498–3502.
- 4 J. R. Miller and P. Simon, *Science*, 2008, **321**, 651–652.
- 5 A. G. Pandolfo and A. F. Hollenkamp, *J. Power Sources*, 2006, **157**, 11–27.
- 6 D. N. Futaba, K. Hata, T. Yamada, T. Hiraoka, Y. Hayamizu, Y. Kakudate, O. Tanaike, H. Hatori, M. Yumura and S. Iijima, *Nat. Mater.*, 2006, **5**, 987–994.
- 7 S. Talapatra, S. Kar, S. K. Pal, R. Vajtai, L. Ci, P. Victor, M. M. Shaijumon, S. Kaur, O. Nalamasu and P. M. Ajayan, *Nat. Nanotechnol.*, 2006, **1**, 112–116.
- 8 K. H. An, W. S. Kim, Y. S. Park, J. M. Moon, D. J. Bae, S. C. Lim, Y. S. Lee and Y. H. Lee, *Adv. Funct. Mater.*, 2001, **11**, 387–392.
- 9 M. M. Shaijumon, F. S. Ou, L. Ci and P. M. Ajayan, *Chem. Commun.*, 2008, 2373–2375.
- 10 M. Toupin, T. Brousse and D. Bélanger, *Chem. Mater.*, 2004, **16**, 3184–3190.
- 11 W. Sugimoto, H. Iwata, Y. Yasunaga, Y. Murakami and Y. Takasu, *Angew. Chem., Int. Ed.*, 2003, **42**, 4092–4096.
- 12 J. M. Miller, B. Dunn, T. D. Tran and R. W. Pekala, *J. Electrochem. Soc.*, 1997, **144**, L309–L311.
- 13 A. Rudge, J. Davey, I. Raistrick, S. Gottesfeld and J. P. Ferraris, *J. Power Sources*, 1994, **47**, 89–107.
- 14 D. A. C. Brownson, D. K. Kampouris and C. E. Banks, *J. Power Sources*, 2011, **196**, 4873–4885.
- 15 W. Choi, I. Lahiri, R. Seelaboyina and Y. S. Kang, *Crit. Rev. Solid State Mater. Sci.*, 2010, **35**, 52–71.
- 16 L. Grande, V. T. Chundi, D. Wei, C. Bower, P. Andrew and T. Ryhanen, *Particuology*, 2012, **10**, 1–8.
- 17 M. H. Liang, B. Luo and L. J. Zhi, *Int. J. Energy Res.*, 2009, **33**, 1161–1170.
- 18 D. S. L. Abergel, V. Apalkov, J. Berashevich, K. Ziegler and T. Chakraborty, *Adv. Phys.*, 2010, **59**, 261–482.
- 19 V. Singh, D. Joung, L. Zhai, S. Das, S. I. Khondaker and S. Seal, *Prog. Mater. Sci.*, 2011, **56**, 1178–1271.
- 20 H. A. Becerril, J. Mao, Z. Liu, R. M. Stoltenberg, Z. Bao and Y. Chen, *ACS Nano*, 2008, **2**, 463–470.
- 21 S. Stankovich, D. A. Dikin, R. D. Piner, K. A. Kohlhaas, A. Kleinhammes, Y. Jia, Y. Wu, S. T. Nguyen and R. S. Ruoff, *Carbon*, 2007, **45**, 1558–1565.
- 22 S. Stankovich, D. A. Dikin, G. H. B. Dommett, K. M. Kohlhaas, E. J. Zimney, E. A. Stach, R. D. Piner, S. T. Nguyen and R. S. Ruoff, *Nature*, 2006, **442**, 282–286.
- 23 M. Pumera, *Chem. Soc. Rev.*, 2010, **39**, 4146–4157.
- 24 Y. Q. Sun, Q. O. Wu and G. Q. Shi, *Energy Environ. Sci.*, 2011, **4**, 1113–1132.
- 25 S. Bose, T. Kuila, A. K. Mishra, R. Rajasekar, N. H. Kim and J. H. Lee, *J. Mater. Chem.*, 2012, **22**, 767–784.
- 26 Y. L. Li, J. J. Wang, X. F. Li, D. S. Geng, M. N. Banis, R. Y. Li and X. L. Sun, *Electrochem. Commun.*, 2012, **18**, 12–15.
- 27 Z. Chen, A. P. Yu, R. Ahmed, H. J. Wang, H. Li and Z. W. Chen, *Electrochim. Acta*, 2012, **69**, 295–300.
- 28 D. Higgins, Z. Chen and Z. W. Chen, *Electrochim. Acta*, 2011, **56**, 1570–1575.
- 29 D. C. Higgins, D. Meza and Z. W. Chen, *J. Phys. Chem. C*, 2010, **114**, 21982–21988.
- 30 H. Wang, T. Maiyalagan and X. Wang, *ACS Catal.*, 2012, **2**, 781–794.
- 31 D. S. Geng, S. L. Yang, Y. Zhang, J. L. Yang, J. Liu, R. Y. Li, T. K. Sham, X. L. Sun, S. Y. Ye and S. Knights, *Appl. Surf. Sci.*, 2011, **257**, 9193–9198.
- 32 H. M. Jeong, J. W. Lee, W. H. Shin, Y. J. Choi, H. J. Shin, J. K. Kang and J. W. Choi, *Nano Lett.*, 2011, **11**, 2472–2477.
- 33 L. Guan, L. Cui, K. Lin, Y. Y. Wang, X. T. Wang, F. M. Jin, F. He, X. P. Chen and S. Cui, *Appl. Phys. A: Mater. Sci. Process.*, 2011, **102**, 289–294.
- 34 P. H. Matter, L. Zhang and U. S. Ozkan, *J. Catal.*, 2006, **239**, 83–96.
- 35 W. S. Hummers and R. E. Offeman, *J. Am. Chem. Soc.*, 1958, **80**, 1339.
- 36 A. P. Yu, I. Roes, A. Davies and Z. W. Chen, *Appl. Phys. Lett.*, 2010, **96**, 253105.
- 37 G. te Velde and E. J. Baerends, *Phys. Rev. B: Condens. Matter Mater. Phys.*, 1991, **44**, 7888–7903.
- 38 G. Wiesenekker and E. J. Baerends, *J. Phys.: Condens. Matter*, 1991, **3**, 6721–6742.
- 39 J. I. Langford and A. J. C. Wilson, *J. Appl. Crystallogr.*, 1978, **11**, 102–113.
- 40 B. Saikia, R. Boruah and P. Gogoi, *J. Chem. Sci.*, 2009, **121**, 103–106.
- 41 K. N. Kudin, B. Ozbas, H. C. Schniepp, R. K. Prud'homme, I. A. Aksay and R. Car, *Nano Lett.*, 2007, **8**, 36–41.
- 42 Z.-S. Wu, W. Ren, L. Gao, J. Zhao, Z. Chen, B. Liu, D. Tang, B. Yu, C. Jiang and H.-M. Cheng, *ACS Nano*, 2009, **3**, 411–417.
- 43 N. Soin, S. Sinha Roy, S. Roy, K. S. Hazra, D. S. Misra, T. H. Lim, C. J. Hetherington and J. A. McLaughlin, *J. Phys. Chem. C*, 2011, **115**, 5366–5372.
- 44 H. B. Wang, T. Maiyalagan and X. Wang, *ACS Catal.*, 2012, **2**, 781–794.
- 45 L. G. Cancado, K. Takai, T. Enoki, M. Endo, Y. A. Kim, H. Mizusaki, A. Jorio, L. N. Coelho, R. Magalhaes-Paniago and M. A. Pimenta, *Appl. Phys. Lett.*, 2006, **88**, 163106.
- 46 C. Zhang, L. Fu, N. Liu, M. Liu, Y. Wang and Z. Liu, *Adv. Mater.*, 2011, **23**, 1020–1024.
- 47 D. Wei, Y. Liu, Y. Wang, H. Zhang, L. Huang and G. Yu, *Nano Lett.*, 2009, **9**, 1752–1758.
- 48 S. van Dommele, A. Romero-Izquierdo, R. Brydson, K. P. de Jong and J. H. Bitter, *Carbon*, 2008, **46**, 138–148.
- 49 D. Qu, *J. Power Sources*, 2002, **109**, 403–411.
- 50 W.-C. Chen, T.-C. Wen and H. Teng, *Electrochim. Acta*, 2003, **48**, 641–649.
- 51 A. Burke, *Electrochim. Acta*, 2007, **53**, 1083–1091.
- 52 L. L. Zhang and X. S. Zhao, *Chem. Soc. Rev.*, 2009, **38**, 2520–2531.
- 53 M. D. Stoller and R. S. Ruoff, *Energy Environ. Sci.*, 2010, **3**, 1294–1301.
- 54 J. Yan, Z. Fan, T. Wei, J. Cheng, B. Shao, K. Wang, L. Song and M. Zhang, *J. Power Sources*, 2009, **194**, 1202–1207.
- 55 A. Rochefort, D. R. Salahub and P. Avouris, *Chem. Phys. Lett.*, 1998, **297**, 45–50.